Terahertz spectroscope using CMOS camera and dispersive optics

Daniel Headland, Robin Zatta, Philipp Hillger, Ullrich R. Pfeiffer

IEEE Transactions on Terahertz Science and Technology
https://doi.org/10.1109/TTHZ.2020.3004516

Terahertz spectroscope using CMOS camera and dispersive optics

Daniel Headland, Robin Zatta, Philipp Hillger, *Student Member, IEEE,* Ullrich Pfeiffer, *Senior Member, IEEE,*

***Abstract*—There is a need to reduce the cost and size of functional terahertz devices, in order to expedite this notoriously under-utilized frequency band toward practical applications. Electronic integrated circuits (ICs) are extremely useful to this end, as they provide a means to achieve miniaturization and mass-production, leveraging the foundries and techniques that have made digital electronics ubiquitous. Although integration of terahertz systems is expected to diminish performance and functionality, the increased number and availability of devices is likely to compensate for such disadvantages. In this work, we develop a terahertz-range spectroscope that combines a CMOS terahertz camera with custom-machined reflective optics. It is noted that the individual pixels of the camera employ incoherent detection, and hence a single pixel is not able to differentiate distinct frequencies. For this reason, the reflective optics are designed to split a terahertz beam into its constituent frequencies, and target each to a different position on the terahertz camera's focal plane array. The required frequency-scanning functionality is provided by a corrugated reflective optic that operates in a manner similar to a curved diffraction grating. The developed spectroscope is experimentally validated, and its functionality agrees closely with simulation. This work provides a pathway to a new generation of compact, low-cost, all-electronic terahertz spectrometers that employ mass-producible silicon ICs for all active components.**

***Index Terms*—Terahertz, Optics, Spectroscope, Spectrometer, CMOS, Diffraction grating, Curved diffraction grating, Camera**

I. Introduction

SPECTRAL analysis is an indispensable capability for numerous applications of terahertz waves [1]–[4]. It is also instrumental in the development of terahertz technology, e.g. for device characterization, to ensure that terahertz sources radiate exclusively in the frequency bands dictated by their standards, and abide electromagnetic compatibility requirements [5], [6]. As such, the widespread availability of terahertz spectrometers will be decisive in the advancement of terahertz engineering. However, current commercially-available terahertz spectrometers are bulky and expensive, and are thus best-suited for use in a laboratory or industrial facility. Examples include laser-driven optoelectronic devices, such as terahertz time-domain spectrometers [7], [8] continuous-wave (CW) systems [9], and FTIR [10]. The necessity of laser excitation is a significant disadvantage for such systems, due to size requirements and power consumption. All-electronic systems are also available, most commonly in the form of millimeter-wave vector network analyzers and spectrum analyzers that are up-converted to the terahertz range by means of extender heads [11], [12], although the possibility of undesired harmonic content in multiplier-chain based sources has the potential to obfuscate spectroscopic analysis. For both laser-driven and mm-wave-driven terahertz spectrometers, device size, cost, and power consumption limit the scope over which they can be utilized. For instance, current terahertz spectrometers cannot readily be deployed for field-testing, or in small-scale independent workshops.

Terahertz integrated circuits (IC) are a viable means to miniaturize and reduce the cost of terahertz systems. Furthermore, they provide a pathway to mass-production, which will subject terahertz technology to economy-of-scale, to reduce costs further. In the past decade, such integrated circuits have gained significant momentum [13], with noteworthy demonstrations including a broadband 1 k-pixel terahertz camera [14], which has facilitated demonstrations of novel applications such as plenoptic imaging [15]. It is challenging to develop single-chip electronic integrated circuit-based spectroscopy devices that exhibit useful bandwidth. That said, there have been demonstrations of noteworthy exceptions, such as the multi-mode antenna demonstrated by Wu et. al. [16]. However, this device required significant calibration and processing to extract frequency information, which limits its scope of viable practical applications.

The aim of this work is the reduction of cost and size of terahertz systems capable of real-time spectral analysis. To this end, we develop external optics to enable broadband incoherent spectroscopy with terahertz-range CMOS cameras. A dispersive optic divides a terahertz beam into constituent colors, which are subsequently imposed upon the aforementioned terahertz camera [14] at different angles. In brief, each frequency band targets a different pixel of the terahertz camera, thereby repurposing the camera for spectroscopy applications, rather than imaging. We concentrate upon a broad range of frequencies centered on 850 GHz for our investigation, as it corresponds to peak sensitivity of the terahertz camera, and substances of interest such as explosives exhibit discernible spectral features in this range [17]–[19]. In comparison to pre-existing terahertz spectroscopy systems, our demonstrated device is low-cost, low power-consumption, compact, and portable, enabling deployment in a broad variety of field environments.

Previously, we have attempted this manner of spatial-spectral analysis using a diffraction grating and a pair of di-

All authors were with the Institute for High-Frequency and Communication Technology, The University of Wuppertal, Wuppertal 42119, Germany, e-mail: ullrich.pfeiffer@uni-wuppertal.de.

Daniel Headland is currently with the Graduate School of Engineering Science, Osaka University, Osaka 560-8531, Japan, e-mail: headland@ee.es.osaka-u.ac.jp.

Manuscript received MMMM DD, YYYY; revised MMMM DD, YYYY.

electric lenses [20]. However, the experimental setup spanned ∼1 m, rendering it unsuitable for practical applications. Additional to that, Fresnel losses and absorption were both highly detrimental to overall signal-to-noise ratio (SNR). Here, we employ reflective optics exclusively, and this significantly reduces such losses. Furthermore, a more-compact optical setup is realized, as the path of the beam is folded in zig-zag fashion. A shorter propagation distance also reduces losses due to atmospheric absorption [21], which increases the spectroscope's SNR.

Currently, the reflective optics that are found in terahertz laboratories are commonly produced by diamond-turning [22] to yield a smooth finish that is highly reflective for visible wavelengths, which are less than 1 μm. However, a terahertz wavelength is between 0.2 and 2 mm for our frequencies of interest, and hence this level of manufacturing precision is not required. Computer-numerical controlled (CNC) milling of aluminum alloys can achieve surface roughness of less than 1 μm under good conditions, and less than 7 μm in more general circumstances [23]. Thus, loss due to roughness ranges from ∼0.1% to 4.2% at 1 THz [24], [25]. We consider this to be an acceptable degree of loss for our purposes, and at significantly reduced cost, and hence we employ CNC milling in the present work.

We successfully confirm that the readout of the terahertz camera does indeed vary with frequency, and conforms closely to expectation. Additional to that, two dispersive optics are manufactured that target different frequency bands. This allows us to demonstrate system modularity; by substituting the dispersive component, whilst leaving the remainder of the device unaltered, we are able to change the targeted frequency range. A tradeoff between device bandwidth and frequency resolution is noted; a dispersive optic that covers a larger bandwidth will in-general exhibit coarser frequency resolution. Thus, it is in-principle possible to exploit the modularity of the developed spectroscope to mediate this tradeoff as-required, although this is not performed in the present study. For both tested frequency bands targeted by dispersive optics developed in this work, we find that the frequency of incident radiation is recoverable over a ∼50% relative bandwidth. The measured efficiency of the bespoke optical subsystem is ∼75% in the vicinity of the terahertz camera's center-frequency, but is degraded away from this frequency. The frequency resolution of the spectroscope is in the order of several tens of GHz.

The developed terahertz optical setup bears strong resemblance to dispersive optical spectrometers, or grating spectrometers, which are well understood at higher frequencies [26]. Additional to that, terahertz-range demonstrations of related grating spectrometer devices have previously been reported [27]–[30], targeting far-infrared wavelengths, and employing detectors such as Golay cells and microbolometer arrays. By contrast, our demonstration is all-electronic, and employs a CMOS IC-based detector array. For this reason, it is better suited for practical applications of terahertz waves. We also target a range of frequencies for which it is possible to realize SiGe IC sources [31], [32]. If such sources were coupled with the spectroscope that is the main subject of this work, it would produce a terahertz spectrometer for which all signal generation and detection is performed using mass-producible ICs.

II. Design

The device that is the main subject of this article is illustrated in Fig. 1(a). It combines a previously-reported terahertz CMOS camera [14] with three reflective optics that are developed in the present work.

A. Terahertz camera

Previously, the design of the terahertz camera has been covered in extensive detail [14], and hence a thorough explanation is unwarranted here. Instead, we provide a superficial overview of salient features of the camera device that are relevant to the present study.

As illustrated in Fig. 1(b),(c) the camera consists of a single chip that is adhered to the base of a 15 mm-diameter hyper-hemispherical high-resistivity float-zone silicon lens. The chip bears a focal plane array (FPA) with 32×32 incoherently operated terahertz direct detectors, or pixels. A single pixel consists of a broadband ring antenna that is coupled directly to a resistive self-mixing circuit, as shown in Fig. 1(d). This circuit essentially converts incident terahertz power into DC voltage, V_{Out}, which may subsequently be converted into a digital signal, and processed with a desktop computer. Peak detector sensitivity occurs at 850 GHz. The chip is implemented in 65-nm CMOS technology, thereby rendering it amenable to mass production, which engenders significant reductions in per-unit cost under high-volume manufacture.

The lens that is coupled to the chip provides high antenna gain to each terahertz detector, improves the front-to-back-ratio of the antenna pattern, and suppresses undesired substrate-modes. It is also the basis for spatial differentiation between adjacent pixels, as illustrated in Fig. 1(b). Put simply, each detector may receive power from a different far-field direction, and this is exploited to perform spectral analysis in the present work.

B. Optical subsystem

This section presents a brief, conceptual overview of the design of the reflective optics. A derivation of the specific required topologies for the desired beam manipulation functionality is included in the Supporting information. This information is omitted in the main text, as it is somewhat tangential to the primary focus of the study.

The optical system, which is illustrated in Fig. 1(a), consists of three metallic reflector dishes; the corrugated dish, the collimator dish, and the reflector dish, where a single block bears the latter two optics. All are aspherical, parabolic reflectors, as opposed circular or spherical geometries. This allows for small f-numbers without spherical aberration, leading to overall device compactness. The operation of the optical subsystem is as follows. A source emits divergent wavefronts, which are planarized by the collimator dish. Subsequently, the reflected beam is made to fall upon the corrugated dish. This optic functions in a dispersive manner, and projects each frequency

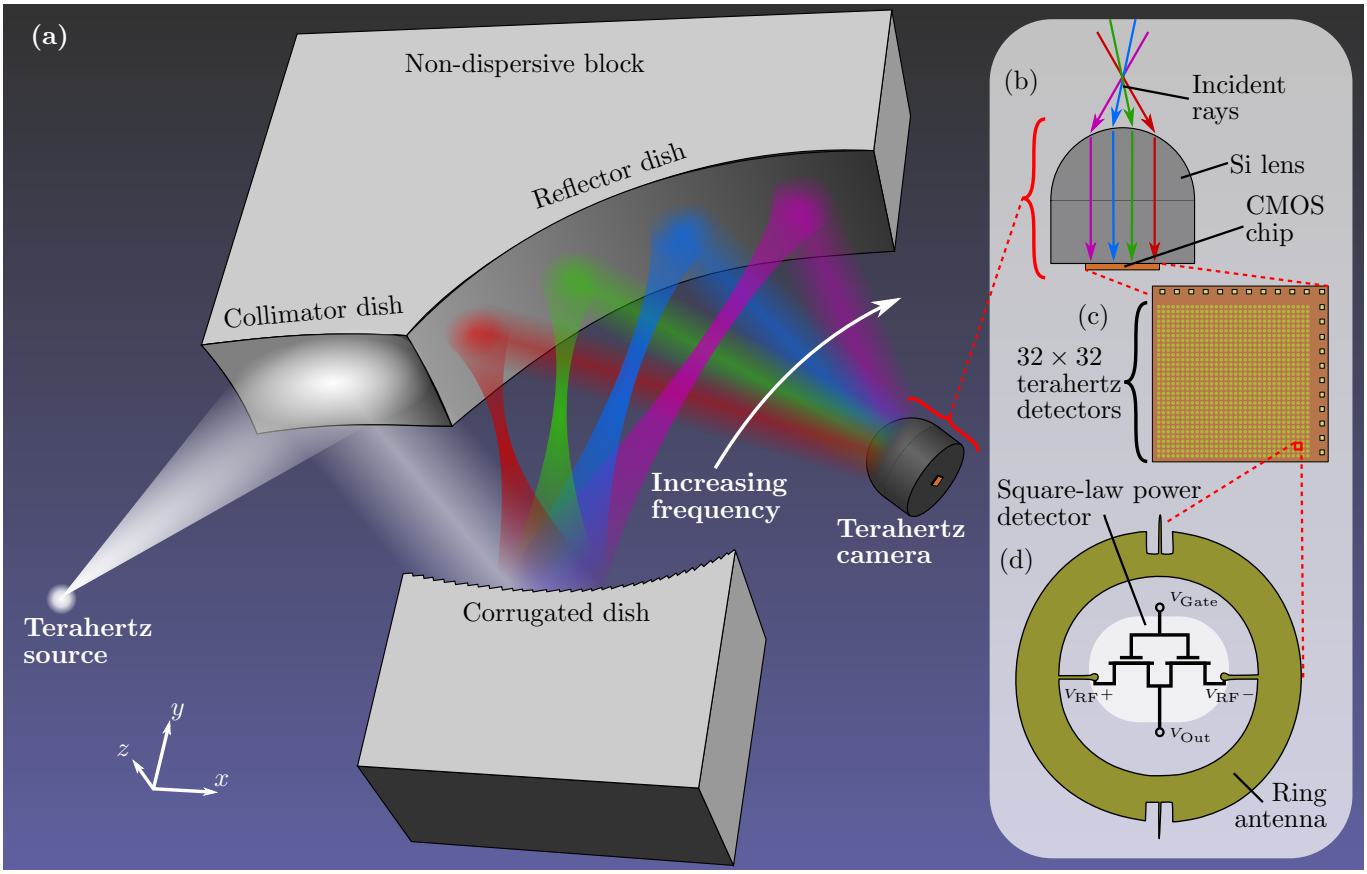

Fig. 1. The dispersive terahertz spectroscope concept, (a) illustration of the overall structure, showing the frequency-dependent behavior of the external reflective optics, (b) the mapping between incident beam direction and focal position on the CMOS chip surface, (c) the FPA on the chip's surface, and (d) the structure of an individual terahertz detector element. The camera is packaged in practice, but this is omitted for clarity.

to a different point in the xy-plane. Thereafter, the reflector dish collects these single-color beams, and redirects them towards the terahertz camera, where they are detected by the central rows of pixels in the FPA. The corrugated dish can be considered a concave-curved diffraction grating, in that it performs frequency-splitting and focusing simultaneously. However, there are some differences to conventional approaches to curved grating design, such as Rowland-circle geometry [33]. In addition to being aspherical, the corrugations of the dish are made aperiodic by directly deriving the local geometry that yields constructive interference at the focus of the desired diffraction order. This approach is preferable because, for aspheric optics of reasonably severe curvature, the dispersion of periodic geometry (i.e. defined parametrically in terms of grating pitch and depth) would be affected by variation in incidence angle across the optic's surface.

The rationale behind the various components of the optical setup is as follows. The terahertz camera is best-suited to receive collimated beams, owing to the high antenna gain that is provided by its silicon lens. These beams must impinge upon the camera at different angles, so as to allow differentiation at the surface of the FPA, as shown in Fig. 1(b). The corrugated dish essentially splits a broadband beam into its constituent colors, which head to different directions. As such, the single-color beams are only coincident at a single point on the surface of this dish. Thus, the reflector dish is required in order to induce the beams to coincide a second time at the camera. However, by re-directing the beams in this way, the reflector dish will also manipulate shape of the individual beam; if they were initially collimated, then the reflector dish would focus them, and focused beams are poorly-matched to the terahertz camera. As such, the individual beams must be diverging when they interact with the reflector dish, so that this dish will collimate the beams rather than focus them. In order to achieve this, the corrugated dish exhibits concave curvature, so as to focus the individual single-color beams in addition to separating them. In other words, the corrugated dish focuses radiation at each frequency to a different point. Finally, in order for the corrugated dish to perform focusing with realistic curvature, it requires collimated incident beams, which necessitates the use of the collimator dish. Thus, all three dishes are required due to the particular characteristics and requirements of the terahertz camera.

The collimator dish interacts with radiation from the modest-aperture terahertz source, which diverges in a spherical manner due to diffraction. As such, this dish must exhibit two-dimensional curvature in order to planarize the incident beam. On the other hand, the beamforming operations of the corrugated dish and reflector dish are restricted to the xy-plane, and hence they need only exhibit curvature in

one dimension. This is because only the central rows of the FPA's pixels is employed for detection, but it is noted that more complicated, two-dimensional frequency-scanning schemes will require curvature in both dimensions.

The optical design process, which is expounded in the Supporting information, is performed in terms of a single centre frequency. The topology of the corrugated dish is such that it projects all incident energy at this frequency directly upwards, to converge upon a point on the y-axis. The focus of the reflector dish coincides with this point, and hence a well-formed collimated beam emerges from the reflector dish. A frequency of 850 GHz is chosen for this purpose, as it corresponds to the maximum sensitivity of the terahertz camera. Away from this frequency, the position of the focus progressively deviates, as is required for the functionality of this dispersive optical device. As such, the focus no longer coincides with that of the reflector dish, and hence the quality of the outgoing collimated beam produced by the reflector dish is decreased. Additional to that, there is a decrease in diffraction efficiency, which is a measure of power lost to un-desired diffraction orders. This is because the phase distribution of the reflected wave deviates from that which is required for all incident energy to appear in the desired diffraction order. Put simply, the performance of the optics is degraded away from the design frequency. That said, this degradation is expected to be sufficiently gradual that the optics will exhibit its desirable functionality over a useful range of frequencies.

III. Optical simulation

Numerical simulations are employed to validate the optical subsystem that is detailed in Section II-B. Specifically, it is desirable to observe the shape of the frequency-scanning beam, and verify that a collimated beam will indeed fall upon the terahertz camera module with a frequency-dependent angle of incidence. In general, optics must be electrically large in order to support the ray-tracing paradigm that their functionality depends upon. Thus, highly accurate methods such as full-wave simulation are unsuitable to model the optical subsystem described in Section II-B. As such, more-approximate methods must be sought. For this reason, we make use of Huygens' principle [34]. This approach approximates electromagnetic waves as a complex scalar quantity, in contrast to their true vector nature, and hence it is also termed "scalar diffraction theory." A given field distribution is treated as equivalent to a dense array of infinitesimal, virtual secondary sources of scalar waves. Each such source is electrically small, and hence it radiates a broad beam for which the complex-valued radiation pattern is modeled straightforwardly. At a distance R from an infinitesimal source of field amplitude A_0, the field strength, A, is given by,

$$A = A_0 \frac{\exp\left(-jk_0R\right)}{j\lambda R} \frac{\left(1+\cos\psi\right)}{2}, \tag{1}$$

where k_0 is the free-space wavenumber, and ψ is the angular deviation of the propagation direction from the Poynting vector.

A few components of this Equation 1 warrant further explanation. In this expression, the $\exp\left(-jk_0R\right)$ term is due to phase that is acquired during propagation, and the $1/(\lambda R)$ term is due to path loss. As the source is electrically small, outgoing wavefronts expand in a spherical manner, and the surface area of a sphere is proportionate to the square of its radius. Thus, outgoing power density decreases in proportion to $1/R^2$, and field magnitude in proportion to the square root of this value. The $(1+\cos\psi)/2$ term is known as the obliquity factor of the virtual source, and is directly analogous to an antenna's radiation pattern. It is at maximum when $\psi = 0$, as radiation is projected into the direction of the Poynting vector, and at zero when $\psi = \pi$, which is the opposing direction. It is noted that the obliquity factor is frequently neglected in cases where it is challenging to determine the direction of the Poynting vector.

In a manner that is analogous to array theory [35], the radiation from a large number of virtual secondary sources is superimposed in order to yield an overall outgoing wavefront. For instance, if the complex-valued scalar field distribution on surface S is defined as $A(S)$, then the field at (x, y, z) may be evaluated as follows,

$$A(x,y,z) = \iint_S A(x_S, y_S, z_S) \frac{\exp(-jkR)}{j\lambda R} \frac{\cos\psi + 1}{2} dS, \tag{2}$$

where (x_S, y_S, z_S) is a given point on surface S, and R and ψ are dependent upon both (x, y, z) and (x_S, y_S, z_S). It is noted that this model does not account for near-field effects, and hence its validity diminishes when close to the surface S.

When modeling the optical system that is presented in this article, Huygens' principle is simplified further. We restrict our simulation to the xy-plane, as this significantly reduces the size of the calculation domain and the required computation time. The three-dimensional surfaces of the reflective optics are thus reduced to two-dimensional curves, representing their shape at $z = 0$. Neglecting the z-axis in this way is equivalent to rendering the physical geometry invariant in the z-direction. A consequence of this is that the Huygens' virtual secondary sources are not point sources, but rather, are infinitely-long lines that are oriented parallel to the z-axis. As such, a Huygens' source radiates a cylindrical wave, rather than a spherical wave, for which the curved surface area is proportionate to the radius, as opposed to the square of the radius. For this reason, the path-loss term in Equation 2 becomes $1/\sqrt{\lambda R}$. Additional to that, we neglect the obliquity factor, and hence the resultant field pattern bears resemblance to an array factor [36], in that it is not multiplied by an individual source's radiation pattern. That said, it is well understood from array theory that the impact of array factor on overall radiation pattern is often stronger than that of an individual source's characteristics. This is especially true in the case of large arrays of broad-beam radiators, as in Huygens' principle. In light of these approximations, Equation 2 takes on the following, simplified

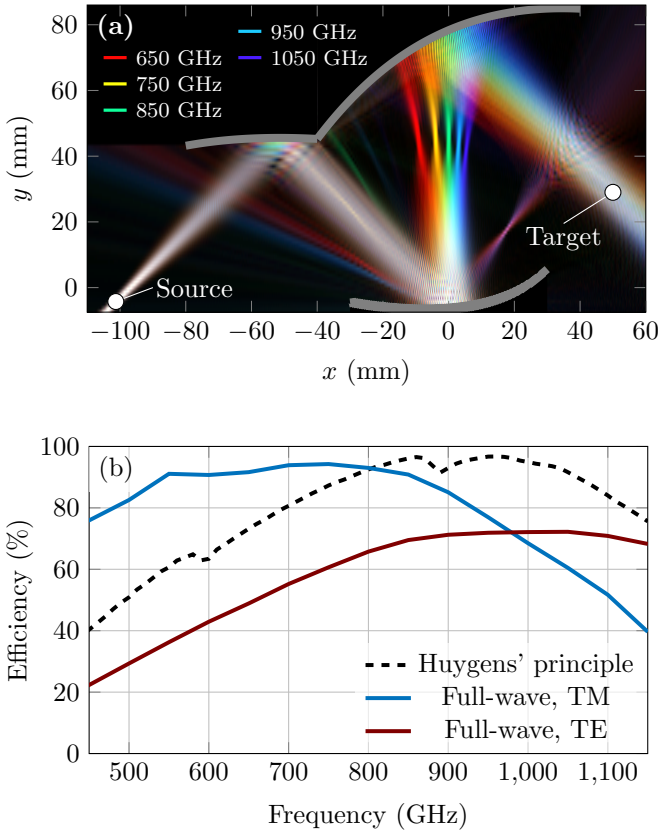

Fig. 2. Simulation results, showing (a) false-color rendition of the results of the Huygens' principle simulation, at five frequencies of interest. These are approximate, two-dimensional simulations that treat the structure as invariant in the z-dimension. (b) Diffraction efficiency of the corrugated dish, calculated using both Huygens' principle and full-wave simulation.

form in our analysis,

$$A(x,y) = \int_C A(x_C, y_C) \frac{\exp(-jkR)}{j\sqrt{\lambda R}} dC, \tag{3}$$

where C is a two-dimensional curve in the xy-plane that represents the surface of a given optical dish. In practice, Equation 3 is calculated numerically, using a Riemann sum.

The source is modeled as a Gaussian beam of $1/e$-width $\sim$1.3 mm, which corresponds roughly to a 26 dB-gain antenna at 850 GHz. Equation 3 is utilized in order to calculate the field distribution that is projected from this source onto the two-dimensional curve that represents the collimator dish. Thereafter, this process is essentially cascaded; the field distribution on the collimator dish is projected onto the corrugated dish, and from there to the reflector dish. Finally, the complex field magnitude in the intervening space is calculated using Equation 3, by superimposing contributions from the source and all reflective dishes. It is noted that, in addition to the above-stated simplifications, this simulation procedure neglects the possibility of backward reflection (e.g. from the corrugated dish to the collimator dish), as well as factors such as material loss and surface roughness. As such, its results approximate, and primarily intended to gain insight into the beamforming functionality of the reflective optics.

In order to represent the geometry in simulation, the x-axis is discretized in steps of 50 µm, which is less than a fifth of a wavelength in our frequency range of interest, and hence it is subwavelength. The 2D curves that describe the dish surfaces are defined as functions thereof. This facilitates direct Riemann-sum calculation of Equation 3 with the exact geometry of the optics, as opposed to approximation by a regular mesh. This simulation model is implemented using GNU Octave.[1] A single simulation typically takes between 120 and 150 seconds using a single core of an i7-6700HQ CPU, in a laptop computer with 16 GB of RAM. In this way, the false-color field plot shown in Fig. 2(a) is generated, as well as a frequency-swept animation that is given in the Supporting information. The false-color field plot in Fig. 2(a) validates that the optical system functions as intended. It is clear that the corrugated dish splits the incident broadband radiation into constituent monochromatic foci at different locations, which are then converted to collimated beams by the reflector dish, and made to converge at the point designated "Target," which is the intended position of the terahertz camera.

A. *Diffraction efficiency*

Diffraction efficiency is estimated by propagating the fields that are reflected from the corrugated dish to a far-field distance of 10 m, and computing the proportion of reflected power from the corrugated dish that is commuted into the desired diffraction order. The results of this procedure are given in Fig. 2(b), showing diffraction efficiency of $\sim$95% in the vicinity of the design frequency.

The scalar nature of our Huygens' principle-based technique does not accurately represent near-field interactions with the corrugations of the dispersive optic, and hence the resulting diffraction efficiency must be treated as approximate. For this reason, full-wave simulations using Ansys HFSS are employed to supplement the investigation of diffraction efficiency. However, due to the large electrical size of the optical subsystem, approximations must be made in order to reduce the size of the simulation to a manageable scope. A Gaussian beam of beamwidth 7.07 mm is employed to represent the fields reflected from the collimator dish, and hence only the surface of the corrugated dish need be considered in the simulation. The size of the dish itself is also reduced to 10×7 mm^2 in the xz-plane. The results are shown in Fig. 2(b), for both TE and TM polarizations. In the TM case, the peak diffraction efficiency is comparable to that which is computed using Huygens' principle, but this peak occurs at a lower frequency. On the other hand, the TE polarization's peak efficiency is reduced to $\sim$72%. The fact that these results differ is an indication of the above assertion that scalar methods are insufficient to compute diffraction efficiency. That said, the accuracy of the full-wave simulations may be impacted by edge effects and imperfect meshing. For these reasons, all results presented in Fig. 2(b) should be treated as approximate.

[1] https://www.gnu.org/software/octave/

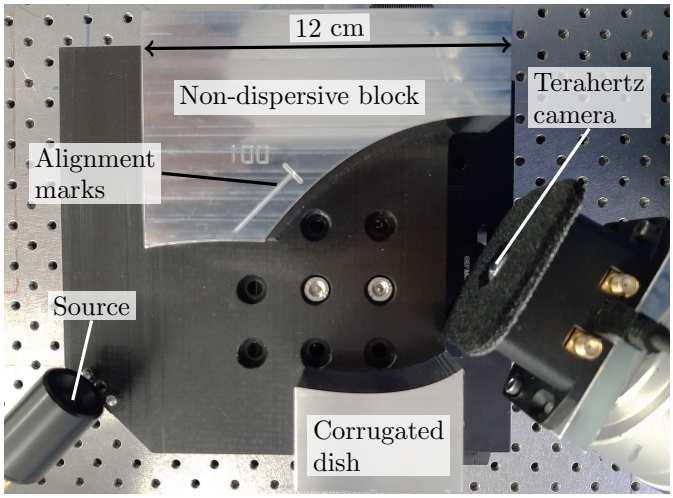

Fig. 3. Experimental setup, showing the custom-machined optics that are developed in this work, as well as the photomixer-based terahertz source, and the camera module that is presented in [14].

IV. Manufacture of Reflective Optics

The reflective optics are fabricated using CNC milling of solid metal. An aluminum alloy (EN AW-5083) is chosen for this purpose, as it is inexpensive, readily machinable, and its appearance exhibits an optical sheen that indicates that it is likely reflective to longer-wavelength terahertz radiation. The result is shown in Fig. 3. The width of the non-dispersive block is indicated in the diagram, and the overall area occupied by the system, including the source, is 15.8cm×16.5cm. Threaded M6 holes are drilled into the underside of both blocks, in order to facilitate mounting on an optics table. The positioning of these M6 holes is such that the non-dispersive block is accurately aligned with the corrugated dish. The non-dispersive block bears marks that also aid the alignment procedure, as they indicate the required position of the source to realize the intended functionality of the optics. The marks resemble a diagonally set "T"-shape, and the source is to be placed at a 100 mm distance from the top-bar of the "T," along a line that is described by the stem of the "T." The width of the non-dispersive block is indicated in the diagram, in order to give an impression of the total size of this terahertz spectroscope device.

It is noted that, as the block that bears the corrugated dish is entirely separate from the non-dispersive block, it may be substituted for a different optic without disturbing any other component of the system. For this reason, we fabricate a second corrugated dish, in addition to the machined optics that are shown in Fig. 3. This second corrugated dish targets a center-frequency of 460 GHz, in order to explore the possibility of a modularity in this terahertz spectroscope, and expand its range of accessible frequencies.

The manufacture of all optics is carried out by a private company that specializes in bespoke manufacture of custom-machined parts.[2] The total cost for all optics is less than €2,000, and it is likely that the cost per-unit will decrease with larger-scale manufacture.

[2]Rapidfacture GmbH

V. Experimental Characterization

A widely-tunable CW source is required to probe the response of the terahertz spectroscope. To this end, we employ photo-mixing terahertz wave generation, whereby the beat signal of a two-color laser signal is extracted by means of a non-linear process, and radiated to free space.[3] This radiated signal's frequency is tunable in the range from 0.035 to 1.32 THz—a five-octave range—and is highly stable, with accuracy in the range from 20–30 kHz. The source's output power varies from ∼300 µW at 0.35 THz to ∼2.5 µW at 1 THz. The TM polarization is used due to its greater diffraction efficiency at the design frequency, as shown in Fig. 2(b).

The generated terahertz power is routed to free-space via a silicon lens. This terahertz source is placed in the position designed by the alignment marks shown in Fig. 3. The terahertz camera is situated at the position that is designated "Target" in Fig. 2(b). It is noted that some manual alignment is required in order to determine the appropriate orientation of the camera, such that radiation at the center-frequency of the corrugated dish is incident upon the center of the camera's FPA.

Initially, the higher-frequency corrugated dish, which is designated "Corrugated dish #1," is deployed in the experiment. The source frequency is swept from 0.4 to 1.2 THz, and camera readout is extracted at intervals of 1 GHz with a 100 ms integration time. A global threshold at a 0 dB SNR level is employed to reduce the impact of noise, which has the potential to obfuscate the pattern of incident radiation on the camera's FPA [37]. An animation that contains all resulting camera-derived images is included in the Supporting information. Following this experiment, the corrugated dish is replaced with the lower-frequency optic (Corrugated dish #2), and the experiment is repeated for a frequency range from 0.1 to 1.2 THz.

A. Spatial-spectral mapping

For each image that is acquired with the terahertz camera, the position of the incident beam's focus on the FPA is estimated by calculating the mean position of incident power over the entire array. Essentially, this is computed as an average of pixel position that is weighted by the power that is incident on each pixel. The calculated position is is converted to an angle of incidence via a geometric argument [15]. The results of this procedure are shown in Fig. 4, for both corrugated dishes, along with a selection of extracted terahertz images. These results show that the direction of the incident beam does indeed scan with respect to operation frequency, as intended.

In order to compare the result to our expectation, the angle of incidence upon the terahertz camera is extracted from the Huygens' principle-based simulation that is detailed in Section III. This is achieved by propagating the fields that are scattered by the reflector dish to a circle at the far-field distance of 10 m, and inspecting the resultant field distribution for the

[3]TeraScan 1550 from Toptica Photonics AG

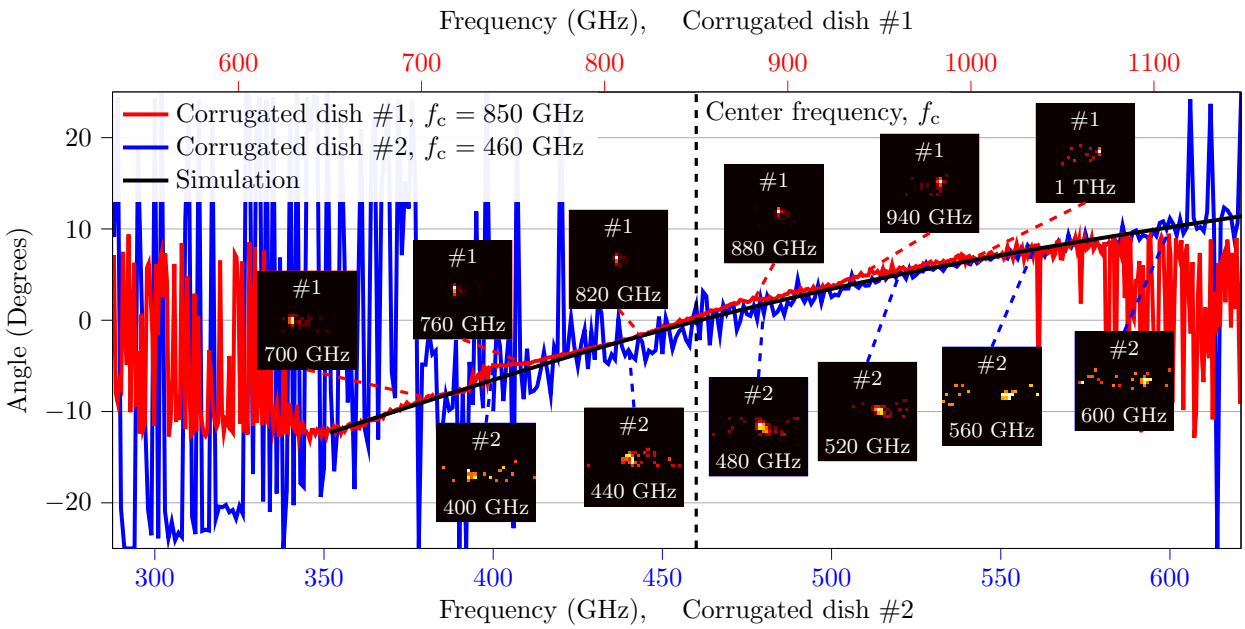

Fig. 4. The spatial-spectral mapping of the spectroscope device, as extracted from the terahertz camera's readout, for both corrugated dishes tested. It is noted that both results are scaled to their respective center-frequency fc, i.e. Corrugated dish #1 is associated with the horizontal axis above the plot, and Corrugated dish #2 with the axis below. Simulation results are also plotted, in order to compare measurement with expectation. Camera readouts at specific frequencies are also included, following noise-gating, in linear-scale of measured terahertz power, where each is normalized to its respective maximum. It is noted that pixels away from the vertical center of the camera's array are not probed for received power, so as to reduce the time required for image acquisition.

direction of maximum radiation. The results of this procedure are also included in Fig. 4, where it can be seen that close agreement with the overall trend of the experimental results is attained. However, there is non-negligible variation in the measured results, especially for frequencies below 500 GHz, and above 1 THz. We ascribe this variation to low SNR as, although it does impact the angle of incidence itself, low SNR will randomize the weighted average from which the reported angle of incidence that is extracted. As the terahertz camera's sensitivity and the diffraction efficiency of the dispersive optic are both highest in the vicinity of ∼850 GHz, degradation of SNR is anticipated away from this frequency. To verify this, the SNR is evaluated as a function of frequency, by comparison of of the maximum intensity pixel and the RMS image noise of the camera. Peak SNR is 28.8 dB and 11.0 dB for Corrugated dishes #1 and #2, respectively. The reduced SNR in the latter case, despite greater source power, is ascribed to reduced camera sensitivity at lower frequencies.

B. Total efficiency

It is desirable to characterize the total efficiency of the custom-machined optical components of the terahertz spectroscope. This includes factors such as astigmatism, mismatch of beam shape to the terahertz camera's sensitivity pattern, spillover, and Fresnel losses due to oblique incidence upon the silicon lens to which the FPA is coupled. As such, total efficiency is not the same as diffraction efficiency, which only considers the proportion of power in the desired diffraction order, and is presented in Section III-A. To this end, the experiments that are illustrated in Figs. 5(a) and (b) are employed. The overall power that is detected by the camera via the optical sub-system is calibrated by a reference measurement that employs a single parabolic reflector dish for collimation. This calibration assumes that the latter dish exhibits near-unity reflection efficiency. The result of this procedure incorporates diffraction efficiency, as well as losses due to surface roughness and Ohmic dissipation. A separate measurement in spectroscope configuration is required for each corrugated dish, and it is noted that all other components of the measurement setup are fixed when these optics are exchanged. In all measurements, source power was set sufficiently low so as to avoid saturation, and camera readout is averaged over a total of 1024 frames. In CMOS terahertz cameras, the detector sensitivity typically scales with $1/\sqrt{N}$, where N denotes the number of frames averaged in this way [37].

The measured efficiency is presented in Fig. 5(c), and it can be seen that the peak efficiency occurs in the vicinity of the design frequency, as expected. Corrugated dish #1 is designed for 0.85 THz, and peak efficiency occurs at 0.79 THz with 74%, and Corrugated dish #2, targets 0.46 THz, yielding peak efficiency of 78% at 0.49 THz. These minor deviations from the design frequencies are likely to misalignment in the experimental setup. It is also noted that the individual camera pixels do not exhibit exactly the same responsivity due to fabrication process variation and deteriorated Gaussicity of off-axis displaced camera pixels [37], [38]. Furthermore, the path length in the setup shown in Fig.5(a) is longer than that in Fig. 5(b), and hence the significant atmospheric absorption of terahertz waves may reduce measured efficiency, especially for frequencies in the vicinity of 560 GHz and 750 GHz [21]. That said, the overall folded propagation length is less than

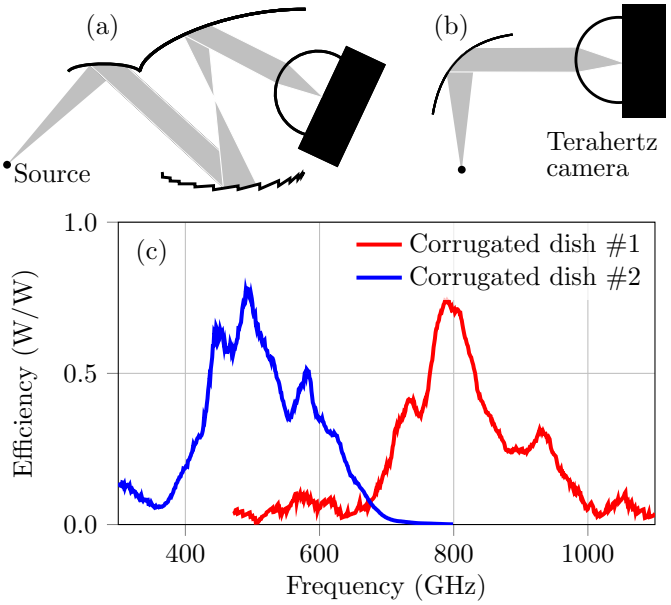

Fig. 5. Overall efficiency of optical subsystem, (a) experimental setup in spectroscope configuration, (b) reference measurement, and (c) resulting measured efficiency of terahertz spectroscopes employing both corrugated dishes.

30 cm, and hence atmospheric absorption is not expected to be a significant factor.

It is evident in the results presented in Fig. 5(c) that efficiency is progressively degraded from its peak value with deviation from the center frequency of the corrugated dish. This contributes to the variation that is observed in Fig. 4. For instance, it is stated above in Section V-A that variation increases markedly for frequencies above 1 THz. It can be seen in Fig. 5(c) that the optical subsection's overall efficiency has decreased to ∼5% in this range. A crossing is observed in the vicinity of 0.68 THz, where both configurations exhibit low efficiency of ∼5%, and hence neither of the corrugated dishes yields high SNR in this range. Thus, it may be beneficial to further leverage the modularity of this spectroscope, and develop a third corrugated dish that targets a center frequency of 0.68 THz in the future. Similarly, the overall usable range of the spectroscope may be extended with additional corrugated dishes. As such, leveraging the modularity of the optical subsystem provides a pathway to realize cost-effective spectrometers that span the 0.15–1.50 THz band.

C. Frequency resolution

We aim to quantitatively estimate the frequency resolution of the spectroscope device that is the main subject of this work, as this is of critical importance to applications of terahertz spectral analysis. For this device, the spatial-spectral mapping that is presented in Fig. 4 is non-linear, and as a consequence, the frequency resolution varies with pixel position. Thus, the frequency response of individual pixels must be evaluated in order to determine their unique frequency resolution. It is not necessary to probe all 1024 pixels in this way, as the incident beam scans horizontally across a central band. For this reason, we compute the frequency-dependent sum of the power in

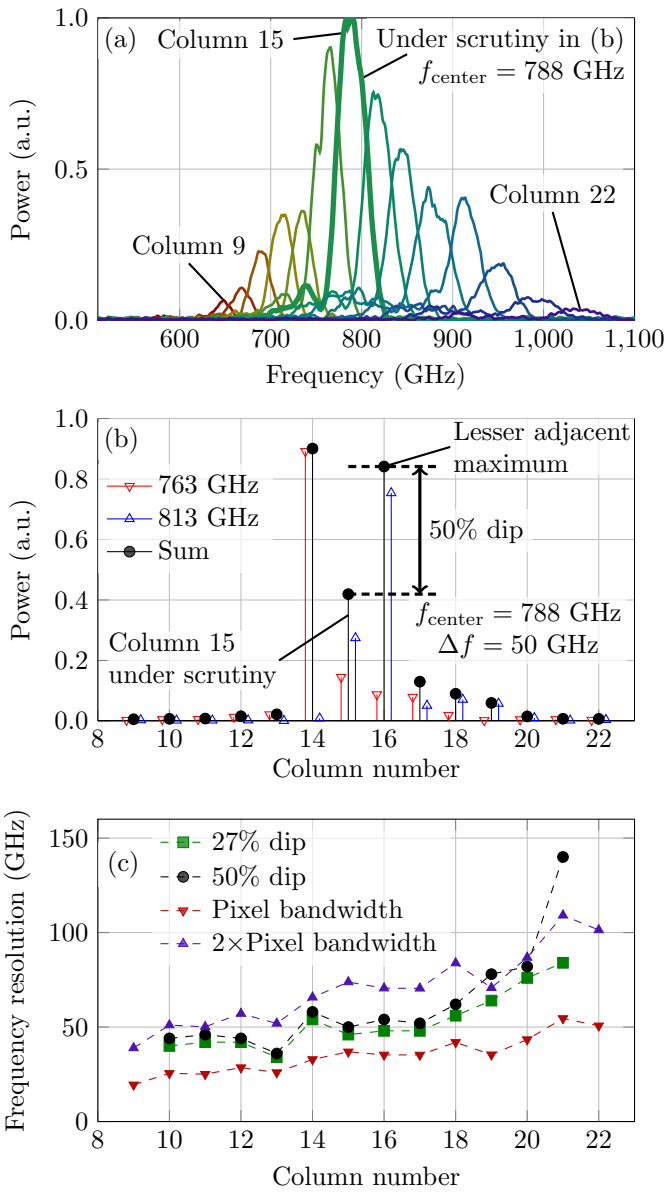

Fig. 6. Analysis of the frequency resolution of the terahertz spectroscope with Corrugated dish #1, showing (a) sum of power incident upon Columns 9 to 22 of the 32×32-pixel array, (b) illustration of the frequency-resolution calculation procedure, using Column 15 with a 50% dip as an example, and, (c) extracted frequency resolution, along with the bandwidth of each pixel, and frequency resolution estimated as a multiple of that bandwidth.

each column of pixels, and the result is plotted in Fig. 6(a) for Corrugated dish #1. Each plotted trace is smoothed [39] in order to remove the influence of variation that arises due to noise and source-power fluctuation. Columns that do not exhibit a discernible peak in power at a given frequency are omitted. In this way, the frequency response of fourteen out of the total thirty-two pixel columns are included in the analysis of frequency resolution. In the context of this study, we aim to extract the frequency resolution directly, without any form of calibration that requires prior knowledge of the spectroscope's response. The plots that are given in Fig. 6(a) are therefore left un-normalized, as this would constitute a form of calibration.

Consider a scenario in which a two-tone signal illuminates

the terahertz spectroscope that is the main subject of this work. The frequency resolution of the spectroscope is defined as the minimum required frequency separation such that the peak associated with each tone may be identified as distinct. In other words, a discernible dip in power between the two tones must be observed in order to distinguish them. This analysis depends on the existence of a representation of the received pixel power under two-tone illumination. However, it would be impractical to directly measure an exhaustive two-tone frequency-sweep in order to generate this, and hence we contrive two-tone signals by summation of the detected power from two single-tone measurements. This approximation carries the assumption that overall received power increases linearly with contributions from different frequencies.

For a given column, the frequency resolution is defined in terms of the two-tone signal that produces a discernible dip at that particular column. This is a criterion that is most commonly associated with the resolution of spatially-separated light sources. It is applicable in this case because, for a spectroscope of this sort, each frequency will appear as a distinct light source. Thus, the spatial resolution of the FPA is essentially the same as its frequency resolution. The center frequency of the column's response is identified as f_{center}, and the frequency resolution is the spacing Δf such that illumination by a two-tone signal at $f_{\text{center}} + \frac{\Delta f}{2}$ and $f_{\text{center}} - \frac{\Delta f}{2}$ will result in the overall power that is detected by that column being below that of neighboring maxima by a specified proportion, such as 50%. The spectroscope is not equally sensitive to all frequencies, and furthermore, source power may vary with frequency. This leads to maxima of different magnitudes. For this reason, the dip is measured relative to the lesser of the two neighboring maxima; otherwise the lower relative power may simply constitute the roll-off of a particularly strong adjacent maximum, rather than a dip. This procedure is illustrated in Fig. 6(b) for a 50% dip, using Column 15 as an example. The center frequency of this column is $f_{\text{center}} = 788$ GHz, and the frequency separation that is required for a 50% dip at this column is $\Delta f = 50$ GHz.

In order to support this extraction procedure, an appropriate relative dip magnitude must be selected. We employ two such values; 27%, which corresponds to Rayleigh's criterion [34], and 50%, which is more severe, and renders dip identification more robust to noise. The results of this procedure are presented in Fig. 6(c), and the details of the algorithm are given in the Supporting information. It can be seen that frequency resolution is in the vicinity of 50 GHz, although this becomes larger for higher frequencies. This is partly owed to the non-linear spatial-spectral mapping that is observed in Fig. 4. Additional factors influence the particularly coarse resolution at Column 21; the power in edge-Column 22 is significantly lower than that of its neighbor, which increases the frequency separation that is required to identify a dip at Column 21. Conversely, Column 13 exhibits finer resolution, as its maximum is not markedly larger than that of Column 12, and hence a dip is identified with lower frequency separation. The frequency resolution is coarser for the 50% deeper dip, although not significantly so, with the exception of Column 21.

The frequency resolution of a grating spectrometer is commonly estimated in terms of the bandwidth of each individual pixel. To this end, pixel bandwidth is extracted from the frequency-response data shown in Fig. 6(a), and the result is given in Fig. 6(c). A multiple of pixel bandwidth is used to estimate frequency separation required to distinguish a two-tone terahertz signal. If the midpoint between these two frequencies is centered upon a given pixel's peak, and the separation is equal to twice that pixel's bandwidth, then each tone will be in the vicinity of the adjacent pixel's maximum. As a result, a dip will be clearly discernible. For this reason, frequency resolution can be estimated as twice the pixel bandwidth, as shown in Fig. 6(c). It can be seen that this is in reasonable agreement with that which is extracted by the method expounded in Fig. 6(b), albeit slightly coarser.

The procedure to quantify frequency resolution was not repeated for Corrugated dish #2, as the extraction of meaningful results was precluded by lower SNR owed to reduced terahertz camera sensitivity for the frequencies targeted by Corrugated dish #2. That said, it is clear from Fig. 4 that the spatial-spectral mapping is in agreement with that of Corrugated dish #1. Thus, we expect that the frequency resolution would be similarly in the range of several tens of GHz if the camera sensitivity were increased.

VI. Conclusion

We have enhanced the functionality of a terahertz CMOS IC by means of custom external optics. Specifically, we have employed three reflective optics in order to convert a terahertz camera from an imaging device into a spectroscope, as a proof of concept. This shows that spectral analysis is achievable with an array of incoherent terahertz CMOS detectors. That said, the achieved frequency resolution was several tens of GHz. Many practical applications of terahertz spectroscopy will likely require finer frequency resolution. In the future, frequency resolution may be enhanced with calibration, interpolation, fitting, and super-resolution imaging techniques [40], as well as advances in CMOS terahertz cameras. Refinements may also be made to the optical sub-system, in order to tailor the frequency-scanning beam to the requirements of the specific application in question.

Only the central rows of the FPA were employed in this work. On the other hand, the full 2D extent of the FPA may be utilized if terahertz frequency-selective surfaces [41] are employed to deflect specific frequency bands out of the xy-plane, after which they can be impinged upon separate corrugated dishes of distinct dispersion characteristics. Thereafter, the subsequent scanning beams can be made to fall upon the camera with dedicated reflector dishes that are angled towards the xy-plane, where they will illuminate separate rows of the FPA that are vertically offset. Improvements may also be made to the feeding structure that impinges terahertz waves upon the collimator dish. There is a risk of aberrations due to phase irregularities in a given sample under test, leading to spurious frequency detection. If, on the other hand, the terahertz waves were passed through a single-mode waveguide following interaction with the sample, then the beam shape will be unchanged, and such phase irregularities will only contribute minor loss.

If practical frequency resolution can be achieved, our proof-of-concept spectroscope may find applications in the characterization of terahertz sources, to ensure that they comply with their regulated output frequency requirements. It will also provide a pathway toward all-electronic terahertz spectrometers that employ silicon ICs for all active components. Such devices will be inexpensive, hand-held, and portable, thereby facilitating rapid terahertz-range testing in a range of field environments. In order to realize this aim, a broadband integrated electronic source is required. This is highly preferable to the photomixing source that is employed in the present work, due to significantly lower power consumption and physical size. Potentially suitable sources have recently been developed in the form of electronic ICs that produce a broadband terahertz pulse in the appropriate frequency range [31]. In the cited work, the detection of the pulse was performed using electro-optical sampling, thereby precluding the possibility of system integration. Thus, the addition of our present work would realize compact and inexpensive all-silicon terahertz spectrometers.

ACKNOWLEDGMENT

This work was partially funded by the German Research Foundation through SFB/Transregio MARIE, project C04. Daniel Headland wishes to thank the Australian Department of Education for providing Endeavour Research Fellowship 6008_2017, which supported his stay in Germany.

REFERENCES

[1] M. C. Beard, G. M. Turner, and C. A. Schmuttenmaer, "Terahertz spectroscopy," *J. Phys. Chem. B*, vol. 106, no. 29, pp. 7146–7159, 2002.
[2] K. Kawase, Y. Ogawa, Y. Watanabe, and H. Inoue, "Non-destructive terahertz imaging of illicit drugs using spectral fingerprints," *Opt. Express*, vol. 11, no. 20, pp. 2549–2554, 2003.
[3] W. Fan, A. Burnett, P. Upadhya, J. Cunningham, E. Linfield, and A. Davies, "Far-infrared spectroscopic characterization of explosives for security applications using broadband terahertz time-domain spectroscopy," *Appl. Spectrosc.*, vol. 61, no. 6, pp. 638–643, 2007.
[4] A. G. Davies, A. D. Burnett, W. Fan, E. H. Linfield, and J. E. Cunningham, "Terahertz spectroscopy of explosives and drugs," *Mater. Today*, vol. 11, no. 3, pp. 18–26, 2008.
[5] D. Morgan, *A handbook for EMC testing and measurement*. IET, 1994.
[6] T. Williams, *EMC for product designers*. Newnes, 2016.
[7] M. Tonouchi, "Cutting-edge terahertz technology," *Nat. Photon.*, vol. 1, no. 2, p. 97, 2007.
[8] C. Jördens, N. Krumbholz, T. Hasek, N. Vieweg, B. Scherger, L. Bähr, M. Mikulics, and M. Koch, "Fibre-coupled terahertz transceiver head," *Electron. Lett.*, vol. 44, no. 25, pp. 1473–1475, 2008.
[9] B. Sartorius, D. Stanze, T. Göbel, D. Schmidt, and M. Schell, "Continuous wave terahertz systems based on 1.5 μm telecom technologies," *J. Infrared Millim. Terahertz Waves*, vol. 33, no. 4, pp. 405–417, 2012.
[10] J. Wagner, H. Seelewind, and P. Koidl, "Optically induced far-infrared absorption from residual acceptors in as-grown GaAs," *Appl. Phys. Lett.*, vol. 49, no. 17, pp. 1080–1082, 1986.
[11] J. L. Hesler, Y. Duan, B. Foley, and T. W. Crowe, "THz vector network analyzer measurements and calibration," in *Proc. ISSTT*, 2010, pp. 23–25.
[12] T. W. Crowe, B. Foley, S. Durant, K. Hui, Y. Duan, and J. L. Hesler, "VNA frequency extenders to 1.1 THz," in *Proc. IRMMW-THz*. IEEE, 2011.
[13] P. Hillger, J. Grzyb, R. Jain, and U. R. Pfeiffer, "Terahertz imaging and sensing applications with silicon-based technologies," *IEEE Trans. Terahertz Sci. Technol.*, vol. 9, no. 1, pp. 1–19, 2018.
[14] R. Al Hadi, H. Sherry, J. Grzyb, Y. Zhao, W. Forster, H. M. Keller, A. Cathelin, A. Kaiser, and U. R. Pfeiffer, "A 1 k-pixel video camera for 0.7–1.1 terahertz imaging applications in 65-nm CMOS," *IEEE J. Solid-State Circuits*, vol. 47, no. 12, pp. 2999–3012, 2012.
[15] R. Jain, J. Grzyb, and U. R. Pfeiffer, "Terahertz light-field imaging," *IEEE Trans. Terahertz Sci. Technol.*, vol. 6, no. 5, pp. 649–657, 2016.
[16] X. Wu and K. Sengupta, "Single-chip source-free terahertz spectroscope across 0.04–0.99 THz: combining sub-wavelength near-field sensing and regression analysis," *Opt. Express*, vol. 26, no. 6, pp. 7163–7175, 2018.
[17] F. Huang, B. Schulkin, H. Altan, J. F. Federici, D. Gary, R. Barat, D. Zimdars, M. Chen, and D. Tanner, "Terahertz study of 1, 3, 5-trinitro-s-triazine by time-domain and Fourier transform infrared spectroscopy," *Appl. Phys. Lett.*, vol. 85, no. 23, pp. 5535–5537, 2004.
[18] H.-B. Liu, Y. Chen, G. J. Bastiaans, and X.-C. Zhang, "Detection and identification of explosive rdx by thz diffuse reflection spectroscopy," *Opt. Express*, vol. 14, no. 1, pp. 415–423, 2006.
[19] J. Chen, Y. Chen, H. Zhao, G. J. Bastiaans, and X.-C. Zhang, "Absorption coefficients of selected explosives and related compounds in the range of 0.1–2.8 THz," *Opt. Express*, vol. 15, no. 19, pp. 12 060–12 067, 2007.
[20] D. Headland, P. Hillger, R. Zatta, and U. Pfeiffer, "Incoherent, spatially-mapped THz spectral analysis," in *Proc. IRMMW-THz*. IEEE, 2018.
[21] Y. Yang, M. Mandehgar, and D. R. Grischkowsky, "Understanding THz pulse propagation in the atmosphere," *IEEE Trans. Terahertz Sci. Tech.*, vol. 2, no. 4, pp. 406–415, 2012.
[22] M. Warren, "Diamond-turned optics manufacturing and precision mechanical metrology," *Optics & Photonics News*, vol. 19, no. 3, pp. 18–21, 2008.
[23] U. Fischer, R. Gomeringer, M. Heinzler, R. Kilgus, F. Näher, S. Oesterle, H. Paetzold, and A. Stephan, *Mechanical and metal trades handbook*, 3rd ed. Europa Lehrmittel, 2012.
[24] Y. Dikmelik, J. B. Spicer, M. J. Fitch, and R. Osiander, "Effects of surface roughness on reflection spectra obtained by terahertz time-domain spectroscopy," *Opt. Lett.*, vol. 31, no. 24, pp. 3653–3655, 2006.
[25] D. Headland, W. Withayachumnankul, M. Webb, H. Ebendorff-Heidepriem, A. Luiten, and D. Abbott, "Analysis of 3D-printed metal for rapid-prototyped reflective terahertz optics," *Opt. Express*, vol. 24, no. 15, pp. 17 384–17 396, 2016.
[26] W. Neumann, *Fundamentals of dispersive optical spectroscopy systems*. SPIE Press, 2014.
[27] R. Lord and T. McCubbin, "Infrared spectroscopy from 5 to 200 microns with a small grating spectrometer," *J. Opt. Soc. Am.*, vol. 47, no. 8, pp. 689–697, 1957.
[28] F. Kneubühl, J.-F. Moser, and H. Steffen, "High-resolution grating spectrometer for the far infrared," *J. Opt. Soc. Am.*, vol. 56, no. 6, pp. 760–764, 1966.
[29] R. Eichholz, H. Richter, S. Pavlov, M. Wienold, L. Schrottke, R. Hey, H. Grahn, and H.-W. Hübers, "Multi-channel terahertz grating spectrometer with quantum-cascade laser and microbolometer array," *Appl. Phys. Lett.*, vol. 99, no. 14, p. 141112, 2011.
[30] N. Kanda, K. Konishi, N. Nemoto, K. Midorikawa, and M. Kuwata-Gonokami, "Real-time broadband terahertz spectroscopic imaging by using a high-sensitivity terahertz camera," *Sci. Rep.*, vol. 7, p. 42540, 2017.
[31] M. M. Assefzadeh and A. Babakhani, "Broadband oscillator-free thz pulse generation and radiation based on direct digital-to-impulse architecture," *IEEE J. Solid-State Circuits*, vol. 52, no. 11, pp. 2905–2919, 2017.
[32] U. R. Pfeiffer, Y. Zhao, J. Grzyb, R. Al Hadi, N. Sarmah, W. Förster, H. Rücker, and B. Heinemann, "A 0.53 THz reconfigurable source module with up to 1 mW radiated power for diffuse illumination in terahertz imaging applications," *IEEE J. Solid-State Circuits*, vol. 49, no. 12, pp. 2938–2950, 2014.
[33] J. Mack, J. Stehn, and B. Edlén, "On the concave grating spectrograph, especially at large angles of incidence," *J. Opt. Soc. Am.*, vol. 22, no. 5, pp. 245–264, 1932.
[34] J. W. Goodman, *Introduction to Fourier Optics*. Roberts and Company Publishers, 2005.
[35] D. Headland, Y. Monnai, D. Abbott, C. Fumeaux, and W. Withayachumnankul, "Tutorial: Terahertz beamforming, from concepts to realizations," *APL Photonics*, vol. 3, no. 5, p. 051101, 2018.
[36] C. A. Balanis, *Antenna theory: Analysis and design*, 4th ed. John wiley & sons, 2016.
[37] R. Zatta, R. Jain, and U. R. Pfeiffer, "Characterization of the noise behavior in lens-integrated CMOS terahertz video cameras," *The International Journal of Terahertz Science and Technology*, vol. 11, no. 4, pp. 102–123, 2018.
[38] D. F. Filipovic, G. P. Gauthier, S. Raman, and G. M. Rebeiz, "Off-axis properties of silicon and quartz dielectric lens antennas," *IEEE Trans. Antennas Propag.*, vol. 45, no. 5, pp. 760–766, 1997.

[39] P. H. Eilers, "A perfect smoother," *Anal. Chem.*, vol. 75, no. 14, pp. 3631–3636, 2003.
[40] R. Zatta, R. Jain, J. Grzyb, and U. R. Pfeiffer, "Resolution Limits in Lens-Integrated CMOS THz Cameras Employing Super-Resolution Imaging," in *Proc. IRMMW-THz*. IEEE, 2019.
[41] A. Ebrahimi, S. Nirantar, W. Withayachumnankul, M. Bhaskaran, S. Sriram, S. F. Al-Sarawi, and D. Abbott, "Second-order terahertz bandpass frequency selective surface with miniaturized elements," *IEEE Trans. Terahertz Sci. Tech.*, vol. 5, no. 5, pp. 761–769, 2015.

Daniel Headland earned his PhD from The University of Adelaide, Australia, in 2017. His thesis, which was titled "Efficient terahertz-range beam control using flat optics," was awarded the Doctoral Research Medal and a Dean's Certificate of Doctoral Thesis Excellence by his *alma mater*. Thereafter, he completed a short-term post-doctoral fellowship at the University of Wuppertal, Germany, where he sought to expand the functionality of advanced terahertz-range CMOS circuits using classical optics techniques. Daniel is currently based at Osaka University, Japan, where his research activities pertain primarily to terahertz photonics using intrinsic silicon, with a focus on waveguides, multiplexers, and antennas to support high-capacity communications applications.

Robin Zatta Robin Zatta received a Bachelor's degree in industrial and electrical engineering, and a Master's degree in industrial and automotive engineering from the University of Wuppertal, Germany, in 2016 and 2018, respectively. During his education, he was a joint Research Fellow with the Institute for High-Frequency and Communication Technology (IHCT), where his research activities included automated experimentation and electromagnetic design.

Robin is currently pursuing a doctoral degree at the Institute for High-frequency and Communication Technology. His research interests include novel applications of CMOS terahertz cameras, and high-frequency analog circuit design in integrated silicon process technologies.

Philipp Hillger (GS'15–M'17) received the B. Sc. and M. Sc. degrees in electrical engineering from the Ruhr-University Bochum, Bochum, Germany, in 2011 and 2014, respectively, and is currently working toward a doctoral degree at the Institute for High-Frequency and Communication Technology, Wuppertal, Germany.

From 2011 to 2013, he was with Intel Mobile Communications, Duisburg, Germany, where he was involved in IC design and system engineering for various wireless standards. His major fields of interest are silicon-based mmWave and THz systems for imaging, sensing, and communication.

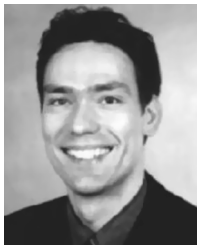

Ullrich Pfeiffer Ullrich R. Pfeiffer (M'02–SM'06) received the Diploma degree in physics and the Ph.D. degree in physics from the University of Heidelberg, Heidelberg, Germany, in 1996 and 1999, respectively.

In 1997, he was a Research Fellow with the Rutherford Appleton Laboratory, Harwell, U.K. From 1999 to 2001, he was a Postdoctoral Researcher with the University of Heidelberg on real-time electronics for particle physics experiments at the European Organization for Nuclear Research (CERN), Switzerland. From 2001 to 2006, he was with the IBM T. J. Watson Research Center, where his research involved RF circuit design, power amplifier design at 60 and 77 GHz, high-frequency modeling, and packaging for millimeter-wave communication systems. In 2007, he led the THz Electronics Group, Institute of High-Frequency and Quantum Electronics at the University of Siegen, Germany. Since 2008, he has been the High-frequency and Communication Technology Chair with the University of Wuppertal, Germany. His current research includes silicon RFICs for mmWave/THz communication, radar, and imaging systems.

Dr. Pfeiffer was the recipient of a European Young Investigator Award in 2007. He was the co-recipient of the 2004 and 2006 Lewis Winner Award for Outstanding Paper of the IEEE International Solid-State Circuit Conference, the co-recipient of the 2006 IBM Pat Goldberg Memorial Best Paper Award, the 2008 EuMIC Best Paper Award, the 2010 EuMC Microwave Prize, the 2012 Jan Van Vessem Award for Outstanding European Paper of the 2012 IEEE International Solid-State Circuit Conference, the 2014 EuCAP Best Paper Award, and the 2017 Microwave Prize. He has been a Distinguished Lecturer of the IEEE Solid-State Circuits Society and the President of the German Association for Electrical Engineering and Information Technology e.V. (FTEI).